Journal of Geophysical Research: Space Physics

RESEARCH ARTICLE
10.1029/2018JA025294

Key Points:
- The first time solar flare response has been investigated in a fully coupled climate model
- September 2005 solar flares affected temperature and composition of the mesosphere and the thermosphere but not the stratosphere
- Solar flare spectra determine the response in the atmosphere

Correspondence to:
J. Pettit,
joshua.pettit@colorado.edu

Citation:
Pettit, J., Randall, C. E., Marsh, D. R., Bardeen, C. G., Qian, L., Jackman, C. H., et al. (2018). Effects of the September 2005 solar flares and solar proton events on the middle atmosphere in WACCM. *Journal of Geophysical Research: Space Physics*, *123*. https://doi.org/10.1029/2018JA025294

Received 31 JAN 2018
Accepted 3 JUN 2018
Accepted article online 15 JUN 2018

Effects of the September 2005 Solar Flares and Solar Proton Events on the Middle Atmosphere in WACCM

J. Pettit[1,2], C. E. Randall[1,2], D. R. Marsh[3], C. G. Bardeen[3], L. Qian[4], C. H. Jackman[5], T. N. Woods[2], A. Coster[6], and V. L. Harvey[1,2]

[1]Department of Atmospheric and Oceanic Sciences, University of Colorado Boulder, Boulder, CO, USA, [2]Laboratory for Atmospheric and Space Physics, University of Colorado Boulder, Boulder, CO, USA, [3]National Center for Atmospheric Research, Boulder, CO, USA, [4]High-Altitude Observatory, National Center for Atmospheric Research, Boulder, CO, USA, [5]NASA Goddard Space Flight Center, Greenbelt, MD, USA, [6]Massachusetts Institute of Technology Haystack Observatory, Westford, MA, USA

Abstract This work investigates middle atmosphere effects of the September 2005 solar flares and solar proton events (SPEs). X-17 and X-6.2 flares occurred on 7 and 9 September, respectively, while two moderate SPEs occurred on 10 and 15 September. Flare ionization and dissociation were calculated in the Whole Atmosphere Community Climate Model (WACCM) using the Flare Irradiance Spectral Model. Proton measurements from the Geostationary Operational Environmental Satellite system were used to compute solar proton ionization. SPEs are shown to have a larger impact than solar flares on the polar stratosphere and mesosphere; however, flares have a larger influence on the sunlit and equatorial lower thermosphere. The two flares differed significantly with respect to photon spectrum. The larger, X-17 flare was stronger during the impulsive phase, while the X-6.2 flare was stronger during the gradual phase. This resulted in the X-17 flare causing more initial ionization but for a shorter duration. The simulated flare impacts also differed because specific wavelengths of the flares influenced the atmosphere above the model top. Model-measurement comparisons show that WACCM captures the overall timing and spatial distribution of the observed electron enhancements, indicating a reasonable simulation of flare and SPE-induced ionization. Both the SPEs and flares caused odd nitrogen increases in the mesosphere. Odd hydrogen produced in the lower mesosphere by the SPEs led to short-lived ozone decreases of nearly 100%. The flares caused small temperature increases in the lower thermosphere but had no effect on the stratosphere.

Plain Language Summary This is the first study to use a global climate model to investigate the effects of solar flares on the Earth's atmosphere from the surface up to about 140 km. The model simulations confirm that a flare's energy spectrum, which differs from flare to flare, determines how the atmosphere is affected. For the flares investigated in this work, which occurred in September of 2005, the simulations show that the solar photons ionized the atmosphere for several hours, causing large increases in electron density. The ionization led to small increases in temperature and also initiated a cascade of chemical reactions that resulted in the production of reactive nitrogen oxides in the mesosphere and thermosphere. There were no significant effects of the flares on the stratosphere. This work is important because it adds to our growing understanding of how impulsive solar events such as solar flares affect the Earth's atmosphere and provides a foundation for understanding their cumulative impacts on the atmosphere and possibly climate.

1. Introduction

Space weather can have considerable impacts on the Earth and the near-Earth environment. In addition to astronaut health and satellite degradation (Lanzerotti, 2013; Turner, 2013), large space weather events can have impacts on the dynamics and composition of the middle and upper atmosphere. Energetic particle precipitation (EPP), the process by which charged particles from the Sun or magnetosphere impinge on the atmosphere, is one example of this (Jackman et al., 1980; Sinnhuber et al., 2012; Solomon et al., 1982; Thorne, 1980). Auroral processes cause routine precipitation of low-energy electrons and protons into the thermosphere; radiation belt processes and solar proton events (SPEs) lead to episodic precipitation of higher-energy electrons and protons into the mesosphere and upper stratosphere. Precipitating particles

ionize and dissociate atmospheric constituents, which results in the production of odd hydrogen (HO_x = H, OH, and HO_2) and reactive odd nitrogen (NO_x = N, NO, and NO_2; e.g., Crutzen et al., 1975; Thorne, 1980). NO_x and HO_x can lead to significant ozone depletion, as well as fluctuations in concentrations of other chemical species in the middle atmosphere (e.g., Crutzen et al., 1975; Jackman et al., 1995; López-Puertas et al., 2005; Randall et al., 1998, 2001, 2005; Solomon et al., 1981).

Solar flares also influence the mesosphere and thermosphere (Donnelly, 1976; Enell et al., 2008; Tsurutani et al., 2009; Woods et al., 2004). Depending on the flare's spectral irradiance and class (e.g., Le et al., 2016; Tsurutani et al., 2005) and the solar zenith angle (Le et al., 2007), photoionization of the atmosphere by solar flares can occur at altitudes from approximately 80 km up through the layers of the ionosphere. The ionosphere is split into different regions. The *D* region is located from approximately 60–100 km and is ionized by hard X-rays ($<$0.1 nm) and Lyman-alpha (121.5 nm), particularly during flares (Donnelly, 1976). The *E* region is located between approximately 100 and 150 km and is ionized primarily by soft X-ray (0.1 nm $\leq \lambda \leq$ 10 nm) and extreme ultraviolet (EUV; $>$10 nm $\leq \lambda \leq$ 121 nm) radiation (Donnelly, 1976). The top layer is the *F* region, which is ionized primarily by radiation in the EUV spectral range between 10 and 100 nm.

In recent years, various global climate models have been used to investigate the effects of SPEs (e.g., Funke et al., 2011; Jackman et al., 2005; López-Puertas et al., 2005). This paper examines the atmospheric effects of SPEs and solar flares using the National Center for Atmospheric Research Whole Atmosphere Community Climate Model (WACCM). The focus is the first 2 weeks of September 2005, when 11 X-class flares and 20 M-class flares erupted from the Sun. Additionally, two medium-sized SPEs occurred at the Earth, peaking on 10 and 15 September (Gopalswamy et al., 2006).

WACCM is a high-top model with a vertical domain that ranges from the surface to approximately 140 km. As such, it allows examination of the effects of solar flares and SPEs on the middle and upper atmosphere. Climate models that include the surface through the upper atmosphere are typically run with a temporal resolution that is too coarse to fully capture phenomena like solar flares. For example, WACCM generally runs with a 30-min time step. In addition, for long-term climate simulations, WACCM uses daily mean solar irradiance and energetic particle forcing (e.g., Matthes et al., 2017). Given that solar flares have typical lifetimes of minutes to hours, the standard model temporal resolution and input cadence are clearly too coarse to accurately study their effects. To address this, a newly developed solar flare data set was created using output from the Flare Irradiance Spectral Model (FISM), a sophisticated solar model with extremely high time and spectral resolution (Chamberlin et al., 2007, 2008). FISM has a 3-s time cadence with 200 wavelengths between 0.5 and 200 nm. The FISM model was used to build a data set that has a 5-min temporal resolution with irradiances across 23 wavelengths in the X-ray and ultraviolet spectral ranges. In addition, Geostationary Operating Environmental Satellite (GOES) data were used to calculate hourly ionization from the SPEs (Jackman et al., 1980; Vitt & Jackman, 1996), rather than using daily averages as are used in the standard model configuration.

The energy for solar flares and coronal mass ejections (CMEs), with which many SPEs are associated, originates from entangled magnetic fields created from both convective plasma within the Sun and circulating plasma near the photosphere (Bastian, 2010). Flares are often characterized by three stages. In the first stage (or prephase), continuous restructuring and destabilization of the magnetic field results in a buildup of a bipolar region in the solar corona prior to a flare; filament eruption also has been noted to occur during this stage (Shibata & Magara, 2011). The second stage is referred to as the impulsive phase, and it is characterized by hard X-ray emission from proton and relativistic electron acceleration (Heyvaerts et al., 1977). The X-17 flare that was released on 7 September showed strong flux during this phase. The last stage is referred to as the main phase or gradual phase. The gradual phase can last up to an hour or longer and is dominated by release of soft X-rays and EUV radiation. Because of the duration of this phase, flares that have strong flux during this phase can be highly geoeffective. The X-6.2 flare that erupted on 9 September showed strong flux in the soft X-ray and EUV spectral regions during this phase.

The location of the eruption on the Sun has a large impact on the flare's geoeffectiveness (Donnelly, 1976; Le et al., 2011; Qian et al., 2010; Tsurutani et al., 2009). In particular, the further from the solar disk center the flare erupts, the more solar atmosphere the photons have to penetrate in order to reach the Earth. The solar atmosphere is a strong absorber of EUV radiation, so EUV photons emerging nearer to the limb are much more

heavily attenuated than EUV photons emerging from the center. However, the solar atmosphere is optically thin with respect to X-rays, so the X-ray flux is less affected by where the flare is located (Donnelly, 1976; Qian et al., 2011); this is particularly true for X-class flares (Le et al., 2011). The two flares examined here erupted from slightly different locations on the limb of the Sun. According to the National Geophysical Data Center (retrieved from https://www.ngdc.noaa.gov/stp/solar/solarflares.html), the X-17 flare erupted at 89° central meridian distance (CMD), while the X-6.2 flare erupted at 62° CMD. As discussed below, differences in the flare spectra were partly a result of the different locations of the flare eruptions.

The most important wavelengths for influencing the upper mesosphere and lower thermosphere are X-rays and EUV (Fuller-Rowell & Solomon, 2010; Solomon & Qian, 2005). The peak ionization altitude for soft X-ray (0.1–10 nm) is about 110 km, whereas the peak ionization altitude for EUV (10–120 nm) is about 160 km. Peak ionization from longer wavelength radiation (>120 nm) ranges from the upper stratosphere near 50 km to the lower thermosphere near 150 km. The enhanced photoionization during a flare causes, among other things, a dramatic increase in electron concentration, an altitude-dependent temperature increase, and an increase of odd nitrogen production in the mesosphere and lower thermosphere.

Several observational studies have attempted to quantify the atmospheric impact of solar flares. Donnelly (1976) was one of the first to evaluate the effects of X-ray and EUV emission on the ionosphere. They found that the EUV impulsive phase of the flare created large amounts of ionization in the *E* and *F* regions. They also found that this response was dependent on the location of the flare eruption on the Sun. The main phase, which was dominated by soft X-rays and EUV radiation, caused ionization mostly in the *E* region between 100 and 130 km. In 2001, a new approach for investigating flares was developed. Afraimovich, Altynsev, Grechnev, et al. (2001) used Global Positioning System (GPS) technology to quantify the total electron content (TEC) variability from solar flares. TEC is a measure of the total column number density of electrons, where one TEC unit (TECU) is 10^{16} electrons/m^2. In a follow-up study, Afraimovich, Altyntsev, Kosogorov, et al. (2001) investigated two solar flares that occurred on 23 September 1998 and 29 July 1999. Both were small, M-class flares with peak observed fluxes of 7.1×10^{-5} W/m^2 and 5.1×10^{-5} W/m^2 in the 0.1- to 0.8-nm channel of GOES. They found that TEC changed by 0.4 TECU for the September flare and 0.5 TECU for the July flare for one line-of-sight measurement. Since the development of this technique, other authors have used similar methods to detect the ionosphere's response to flares. Liu et al. (2006) looked at several strong flares during the early 2000s using the GPS TEC observations. They found a linear relationship between the flare intensity at the X-ray wavelengths and the variation in TEC. Tsurutani et al. (2005) looked at the Halloween storms, which took place in late October and early November in 2003, as well as the Bastille Day event in July of 2000. They found that the spectral variability of the flares has a large effect on the change in TEC. The 28 October 2003 flare was measured at an X-17, whereas the 4 November 2003 flare was measured at a minimum of X-28. Despite this, the X-17 flare produced a TEC increase of ~25 TECU, while the X-28 (at least) flare caused an increase of only 5–7 TECU. The differences were attributed to the fact that the X-28 flare showed a larger hard X-ray increase but a smaller EUV and soft X-ray increase than the X-17 flare due to the respective flare locations on the Sun. The X-28 flare erupted from the right-hand limb of the Sun, whereas the X-17 flare was more centralized, resulting in a high flux in the EUV and soft X-ray.

Several ionosphere/thermosphere modeling studies have been performed to investigate the effects of flares on the thermosphere and ionosphere. Meier et al. (2002) and Huba et al. (2005) investigated ionospheric effects from the 14 July 2000 *Bastille Day* flare. Using the SAMI2 model, Meier et al. (2002) calculated 40% increases in *F* region electron density from a 50% increase in EUV radiation. Using the SAMI3 model, Huba et al. (2005) calculated increases of ~7 TECU in the middle and low latitudes, which compared reasonably well with GPS and TOPEX data. Pawlowski and Ridley (2011) modeled two flares during the Halloween storms on 28 October and 6 November in 2003. Using the Global Ionosphere Thermosphere Model, they found large thermosphere density increases on both the dayside and nightside of Earth. They also showed that most of the energy from flares is deposited below 200 km. When the energy is absorbed at these altitudes, the thermosphere expands upward, bringing the density increases upward with it. This results in large density increases below 400 km. Huang et al. (2013) used the Thermosphere-Ionosphere-Electrodynamics General Circulation Model and included FISM. They showed that the flare spectrum has a large influence on the thermosphere and ionosphere response. The EUV response to the 28 October 2003 flare was largest in the upper thermosphere (~400 km), while the global solar heating was strongest for the X-ray wavelengths.

Table 1
Summary of Simulations Performed

Baseline	None	None	Daily
SPE	Hourly	None	Daily
Flare	None	5 min	Daily
Fully forced	Hourly	5 min	Daily

Note. The time cadence of each of the input files is shown in the cells. SPE = solar proton event.

CMEs often accompany large solar flares. In fact, 90% of X-class flares are associated with CME eruptions (Schrijver, 2009). Although both events are driven by variations of magnetic field strength, CMEs accelerate the overlying plasma in the solar corona, causing large fluxes of energetic particles to be launched into space. CMEs often begin when magnetic flux tubes form in the solar corona; the CME is released when these tubes erupt. The plasma contained within the tubes can be accelerated to speeds as high as 2000 km/s in directions perpendicular to the magnetic field, launching energetic particles into the heliosphere (Hudson, 2010). Sometimes, these particles are directed toward the Earth and cause SPEs, as occurred in September of 2005. The influence of SPEs on the atmosphere has been investigated thoroughly over the last few decades from both a modeling and observational perspective. As reviewed by Jackman et al. (2006), SPEs have been observed to cause large increases in odd hydrogen and odd nitrogen in the polar middle atmosphere, which can lead to significant ozone loss. Jackman et al. (2008) included the September 2005 time period in a study that investigated the short and medium-term effects of SPEs. Using WACCM3 (WACCM version 3), they found that 1.5 Gmol of total odd nitrogen (NO_y) was created from 7 to 17 September 2005, which makes this the 17th strongest SPE period, in terms of NO_y production, since 1963 (Jackman et al., 2008, 2014).

2. Model Description

WACCM is a high-top configuration of the National Center for Atmospheric Research Community Earth System Model (Hurrell et al., 2013). The *high-top* refers to the uppermost level of the atmospheric component, which extends into the thermosphere, making WACCM ideal for studying atmospheric effects from EPP. WACCM version 4 was used in this study and followed the protocols defined for the Chemistry-Climate Model Initiative (Eyring et al., 2013). WACCM is based on the Community Atmospheric Model, version 4, which is on a hybrid-sigma coordinate system with 66 pressure levels from the surface extending to 5.1×10^{-6} hPa. The vertical resolution is 1.1 km in the troposphere, 1.1–1.4 km in the stratosphere below 30 km, 1.75 km from 30 to 50 km, and 3.5 km above 65 km. The horizontal resolution of WACCM4 is 1.9° × 2.5°. The chemistry module in WACCM derives from the Model for Ozone and Related Chemical Tracers, version 3, which is discussed in detail by Kinnison et al. (2007), with updates described in Solomon et al. (2015). The simulations used in this study applied the *Specified Dynamics* WACCM (SD-WACCM) mode (Brakebusch et al., 2013; Marsh et al., 2013). SD-WACCM uses reanalysis data from the Modern-Era Retrospective Analysis for Research and Applications to nudge the meteorological conditions in the model to match actual meteorological conditions for the dates of the simulation (Rienecker et al., 2011). That is, at every time step SD-WACCM calculates new wind and temperature fields by taking 99% of the calculated model data and 1% of the meteorology data. The nudging in this study occurs from the surface to approximately 40 km. The nudging is linearly reduced from 40 to 50 km, where the model becomes free-running (not nudged). Using SD-WACCM also increases the number of pressure levels from 66 to 88. Typically, WACCM is run with a 30-min time step, but for the simulations presented here, the model time step was reduced to 5 min to better resolve the flare effects. Sensitivity studies showed that in the absence of flares or SPEs, reducing the time step to 5 min had negligible impact on the middle atmosphere. Switching to the 5-min time step led to some increases in clouds in the troposphere, mainly in the equatorial region, but differences between the two model simulations above the tropopause were insignificant.

3. Numerical Experiments

The two primary flares that were investigated in this study differed substantially in both their measured strength and their influence on the atmosphere. The flare that occurred on 7 September was measured at X-17, whereas the flare on 9 September was only X-6.2. The first flare was located on the far western limb of the Sun at 89° CMD, while the X-6.2 flare erupted at 62° CMD. In order to best capture the effects from the solar flares, both WACCM and the input data needed to have high temporal resolution.

For this study, four simulations were performed (Table 1). The first was a baseline simulation where no forcing from SPEs or flares was applied. The second simulation was forced just by SPEs, and the third was forced just

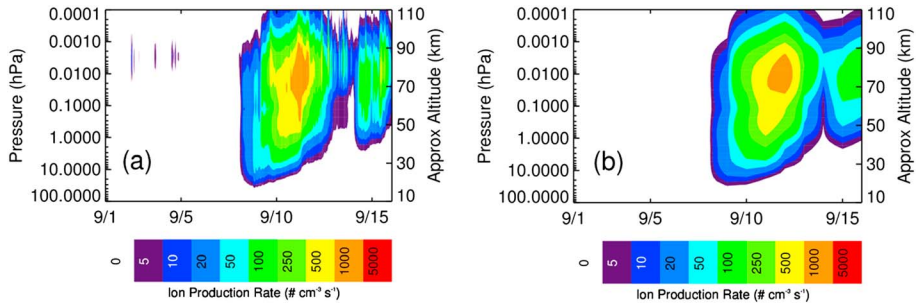

Figure 1. Solar proton event ion production rates as a function of pressure using an hourly time cadence (a) and a daily time cadence (b) for September 2005.

by flares. The fourth was the fully forced simulation that contained both SPEs and flares. All simulations were also forced with daily aurora input, based on the parameterized auroral oval of Roble and Ridley (1987). Input values of proton fluxes for the SPEs were taken from GOES measurements. A detailed description of how the proton fluxes are input into the model is available in Vitt and Jackman (1996). In previous work, hourly proton fluxes were binned into daily averages before the ion production rates were calculated (Jackman et al., 2008, 2009). In the simulations with solar proton forcing presented here, the calculation of ion production rates used hourly, not daily, proton fluxes. Figure 1 shows the difference between the hourly and daily ion production rates. The reduced time cadence (Figure 1a) shows a more detailed and accurate portrayal of the SPEs than the daily time cadence.

The reduced time step in the model was coupled with high time resolution solar data from FISM (Chamberlin et al., 2008). FISM is a solar spectral irradiance empirical model that uses observational data from the GOES X-ray measurements, the Thermosphere Ionosphere Mesosphere Energetics and Dynamics Solar Extreme ultraviolet Experiment (Woods et al., 1994) and the Solar Radiation and Climate Experiment Solar Stellar Irradiance Comparison Experiment (Rottman et al., 1993). It includes wavelengths from 0.5 to 200 nm at 1-nm spectral resolution with a 3-s time cadence. A more complete discussion of the FISM algorithm for both daily cadence and flare effects can be found in Chamberlin et al. (2008). For the flare simulations included in this study, the FISM data were processed into 5-min averages at 23 wavelengths. For the other simulations, the short-lived flares were removed and the FISM data were reduced to daily averages. The importance of the high time cadence of the flare input is illustrated in Figure 2. This figure shows the irradiance in the wavelength bin centered on 1.3 nm during the flare period using the 5-min (black solid) and daily averaged (purple dashed) time cadences, as well as the daily averaged irradiance with the flare removed (red dashed). The 1.3 nm, soft X-ray wavelength was chosen in Figure 2 because flares emit copious amounts of radiation at this wavelength during both the impulsive phase and the main phase. Thus, it is a good indicator for flare strength and flare duration. It can be seen clearly that the 5-min cadence is needed to fully capture the irradiance variability during the flares.

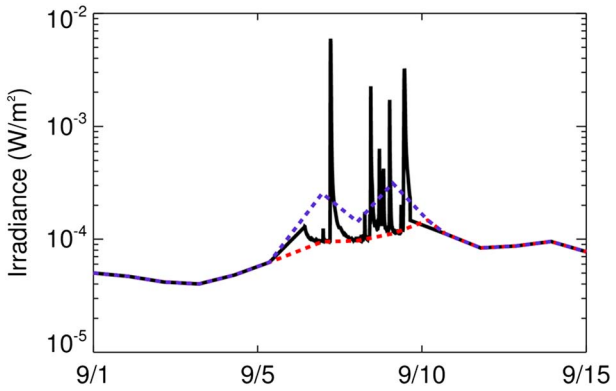

Figure 2. Flare Irradiance Spectral Model irradiance for 1–15 September 2005 at 1.3 nm with a 5-min time cadence (black, solid) and daily time cadence (purple, dashed), and at a daily time cadence with the flares removed (red, dashed).

Figure 3 shows the irradiance at various wavelengths for both flares as calculated by FISM. It is clear from Figures 3a and 3b that the 7 September flare (black line) was a faster-rising, shorter-duration flare compared to the 9 September flare (red line). The 7 September flare began at 17:17 UT, with a flare peak at 17:40 UT. Despite being larger according to the flare class (X-17), the EUV flux enhancement (panels c and d) from the 7 September flare was smaller than that of the 9 September flare, which began at 19:13 UT, since the X-17 flare was located closer to the solar limb than the X-6.2 flare. At 85.5 nm (not shown), the irradiance enhancement from the 9 September flare over the first 4 hr was 25% more than that of the 7 September flare. Much of the EUV energy is deposited at altitudes above the top boundary of WACCM (Solomon & Qian, 2005). However, for wavelengths longer than 100 nm, which are absorbed within the WACCM vertical domain,

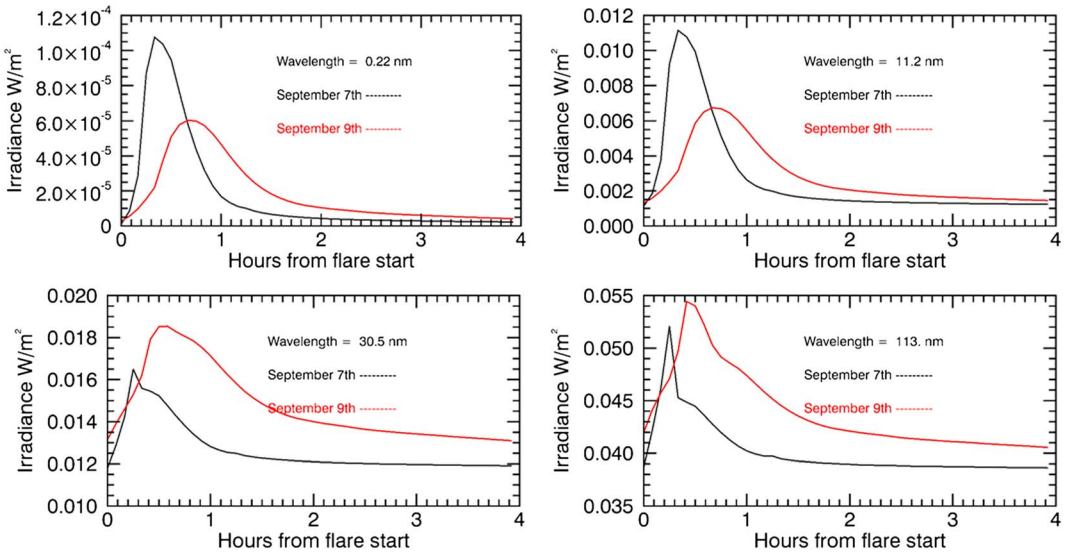

Figure 3. Flare irradiance at various wavelengths in Flare Irradiance Spectral Model, from the 7 and 9 September flares.

the flux from the second flare is much larger than from the first flare. This should result in larger impacts on electron density and odd nitrogen production in the 9 September flare simulation.

4. Results and Discussion

An increase in electron concentration is one of the primary consequences when solar flare radiation reaches the Earth. Significant photoionization occurs as photons strike the dayside of the Earth, with the ionization altitude dependent on the flare spectrum. Figure 4 illustrates the difference in electron number density between the simulation that included flares and the baseline simulation from 1 to 15 September 2005. The top panels (a–c) show the values for the baseline simulation, with the middle and bottom panels showing the electron number density differences (flare minus baseline) in units of % and # electrons/m^3, respectively. Panels (a), (d), and (g) show the Northern Hemisphere (NH) polar average (60–90°N), panels (b), (e), and (h) show the Southern Hemisphere (SH) polar average (60–90°S), and panels (c), (f), and (i) show the equatorial average (30°S–30°N). Individual flares are evident in the plots as vertical stripes between 7 and late on 9 September. Electron increases in the equatorial region (panels f and i) are larger than in either of the polar regions, which is expected since the solar zenith angle is smaller in the equatorial region. Similarly, electron increases in the late NH polar summer (left column) are higher than in the late SH polar winter (middle column). Since the month of interest is September, the NH receives more light from the Sun than the SH, resulting in higher increases in the NH. The maximum number density differences, all of which are associated with the large X-17 flare on 7 September, are 7.4×10^{10} e^-/m^3 in the polar NH at approximately 110 km, 2.5×10^{10} e^-/m^3 in the polar SH also at 110 km, and 1.1×10^{11} e^-/m^3 in the equatorial region at 100 km. The electron number density increases are quite brief in the lower thermosphere (above ~100 km) and last only a few hours, but they reach differences of well over 500% relative to the baseline simulation. The electron increases in the mesosphere (~60–90 km) persist longer than in the thermosphere. It is likely that this is caused by faster recombination of the dissociated electrons in the thermosphere than in the mesosphere. One of the primary recombination pathways for electrons is through combination with NO^+. NO^+ concentrations increase significantly in the thermosphere, which results in more rapid recombination above the mesopause; in the mesosphere, there is less NO^+ available for recombination, resulting in longer lifetimes of the free electrons. Small increases on the order of 10^8 e^-/m^3 can be seen for several days after the solar flares between 70 and 100 km. Electron number densities remained elevated for less time after the strongest flare, which occurred on 7 September, than after the second strongest flare, which occurred on 9 September. The 9 September flare had a longer decay time during the gradual phase, resulting in significantly more EUV radiation; consequently, electron density increases lasted longer. Figure 4 also shows small differences ranging from 0% to 1% above 100 km after 10 September. Since no flares are represented in the model at this time, we attribute these subtle differences to internal variability in the model.

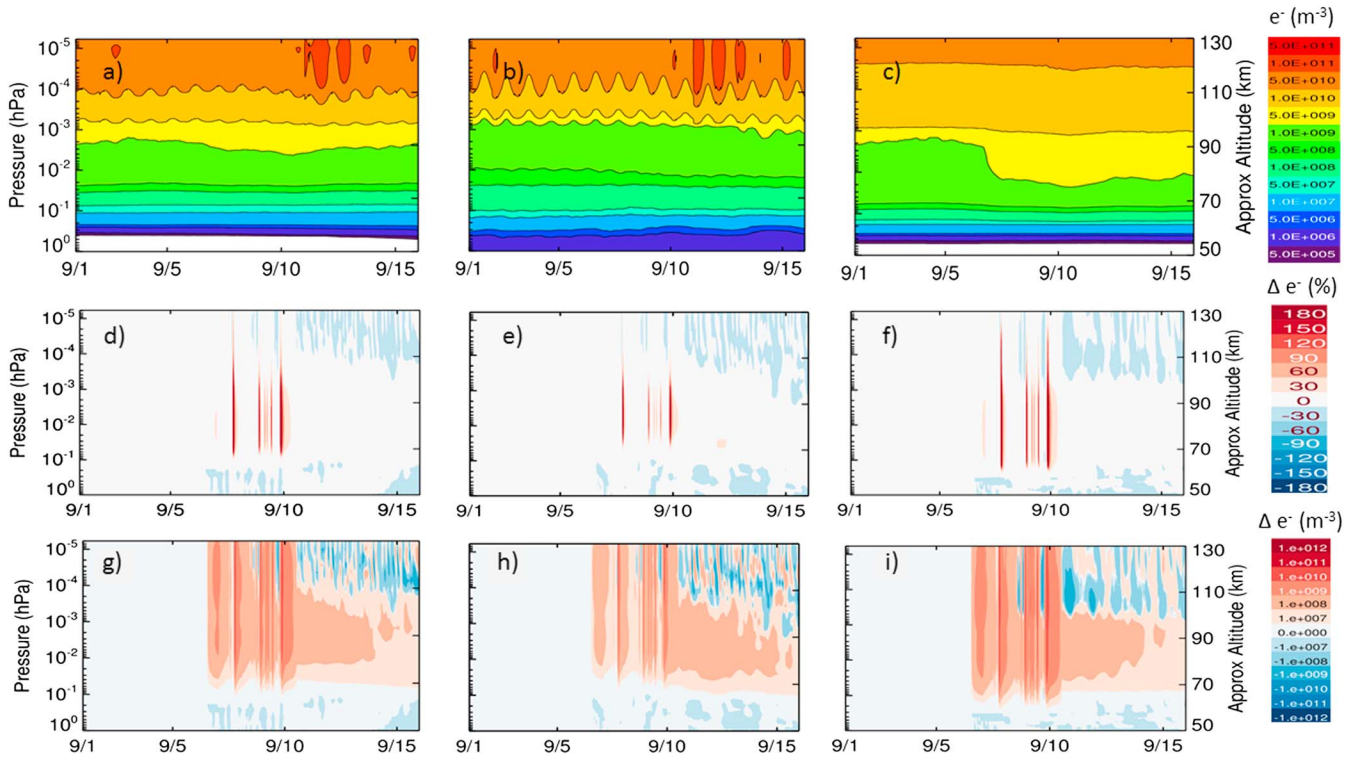

Figure 4. Electron number density background from baseline simulation (top row) and differences in percent (middle row) and number density (bottom row) between the flare simulation and the baseline simulation (flare − baseline) in the Northern Hemisphere (60–90°N; d, g), Southern Hemisphere (60–90°S; e, h), and equatorial region (30°S–30°N; f, i).

Figure 5 shows Mercator maps of the effects of the 7 September X-class flare for electron number density (top), temperature (rows 2 and 3), and NO_x mixing ratio (bottom). All plots correspond to a pressure level of 10^{-4} hPa (~110 km), except for those in row 3, which correspond to 2.7×10^{-5} hPa (~125 km). We found 10^{-4} hPa to be ideal for illustrating the variations during solar flares because this is a level where effects from all variables are seen, but we added 2.7×10^{-5} hPa for temperature because the effects are more prominent. The left column shows the baseline simulation values for each variable at 17 UT on 7 September. Other columns show 30-min averaged differences between the flare and baseline simulations in 2-hr time increments beginning at t_0 = 18 UT.

As expected, once the flare peaks, large electron number density differences can be seen exclusively on the dayside of the Earth (inside the terminator). Increases relative to the baseline of between 100 and 500% are found during the peak on the dayside. After 2 hr, the electron density difference is reduced by a factor of 10, to 10–50% increase from the background. After 4 hr, the electron density difference is reduced to less than a 10% increase relative to the background at high solar zenith angles, with slightly higher increases approaching the terminator. Note that electron differences only appear inside the terminator, which is evidence of the short lifetimes of electrons at this altitude. Unlike the electron enhancements, the average temperature differences from the baseline simulation are highest beginning an hour after the peak of the flare and remain elevated for a few hours at the longitudes where the flare originally hit the Earth. These temperature differences, which are caused by the heating of the thermosphere due to enhanced ionization, are altitude dependent. At 110 km, the temperature differences are 2–3 K. At 125 km, they are as high as 10 K, while at both altitudes the effects remain at the location of the initial flare. In the NH near 70–80°N latitude and 280°–340°E longitude, there are small temperature decreases of between 2 and 8 K (depending on altitude) that we believe are due to model internal variability. The bottom panels show the NO_x differences from the baseline simulation for the same time period. The peak NO_x production follows the similar pattern as the temperature changes, with a slight delay from the peak of the flare of an hour. Like temperature, NO_x produced by the flare is not transported significantly beyond the production region during the first 3 hr. The weakened ionization following the peak of the flare correspondingly produces considerably less NO_x.

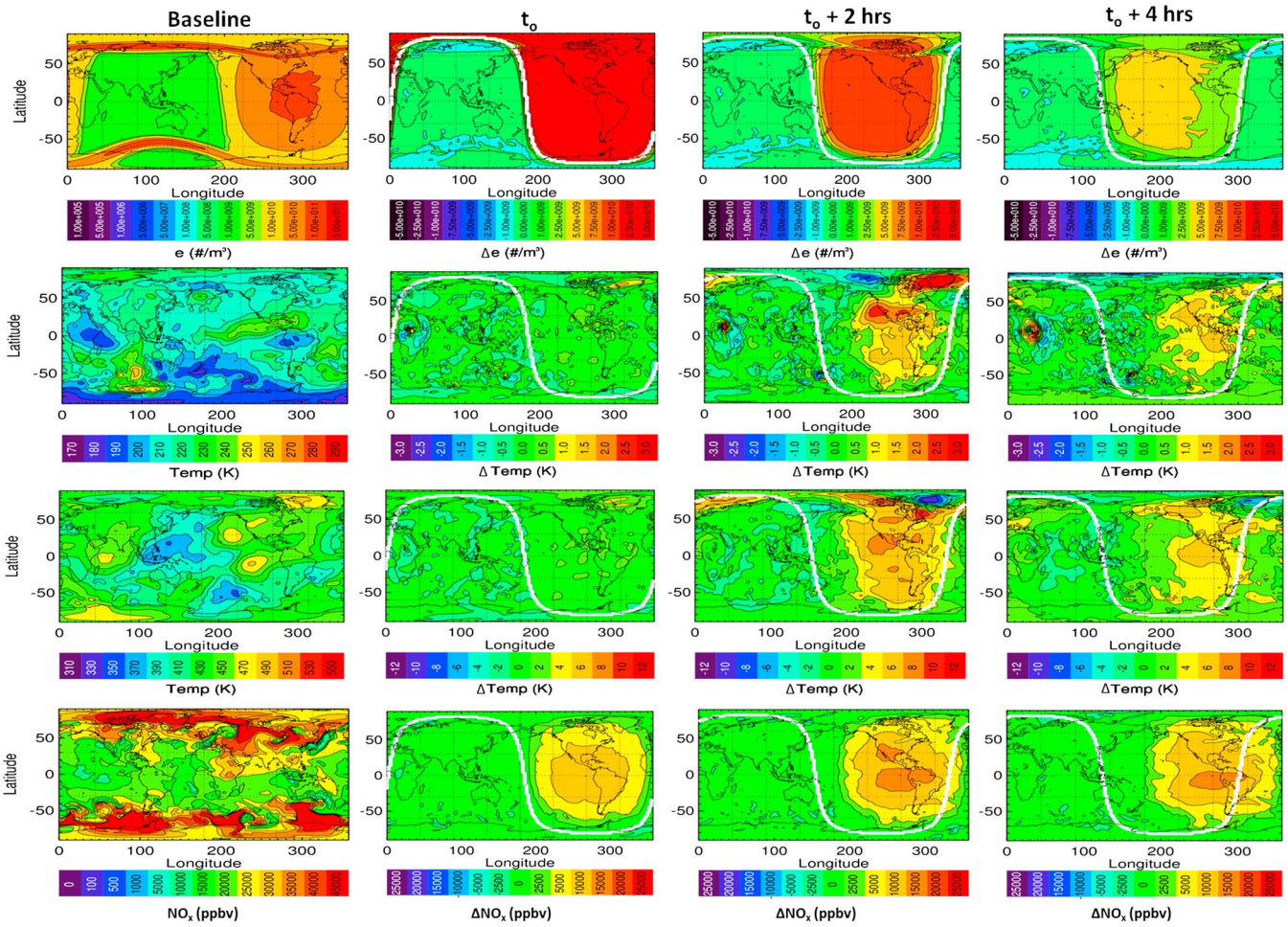

Figure 5. Effects of the 7 September 2005 solar flare on (row 1) electron number density at ~110 km, (row 2) temperature at ~110 km, (row 3) temperature at ~125 km, and (row 4) NO_x at ~110 km. Left column: Maps of baseline simulation values on 7 September at 17 UT. Columns 2–5: Differences between the flare and baseline simulation (flare minus baseline) beginning at t_0 = 18 UT. White contour in columns 2–4 is the terminator (solar zenith angle 90°). Additional gray contours in top row are provided to show levels through 1.8×10^{11} m^{-3}. The black box on the t_0 electron density plot indicates the geographic region for which results are presented in Figure 10.

Figure 6 is analogous to Figure 5 but for the X-6.2 flare that occurred on 9 September. The baseline simulation background values on the left panels are shown for 19 UT; the difference plots begin at t_0 = 20:30 UT. Many of the differences are similar in character to, but larger than, those in Figure 5, except initial electron production. The top plots show that the electron density enhancements are slightly smaller than for the previous flare during the peak but last significantly longer than in the previous flare. Four hours past the peak of the flare, we still see enhancements of 100% relative to the baseline simulation. As explained below, that the second flare was longer in duration led to more overall ionization by the X-6.2 flare on 9 September than by the X-17 flare on 7 September. The peak temperature differences at 125 km, which reach as high as 12 K, occur 2 hr after the flare's peak. This increase is 20% higher than in the previous flare. However, at the lower altitude of 110 km, the temperature difference is not as recognizable. The temperature increases are more localized and not as widespread as in the previous flare. The NO_x differences show larger increases that last longer than in the first flare; NO_x differences greater than 100% from the baseline simulation last 4 hr after the flare begins.

Figure 7 shows the time series of NO_x (a, c) and HO_x (b, d) mixing ratio differences (%) between the forced simulations and the baseline simulation for the NH polar region from 60°N to 90°N. Figures 7a and 7b give the differences between the SPE-forced simulation and the baseline simulation, and Figures 7c and 7d show the differences between the flare-forced simulation and the baseline simulation. The larger of the SPEs began

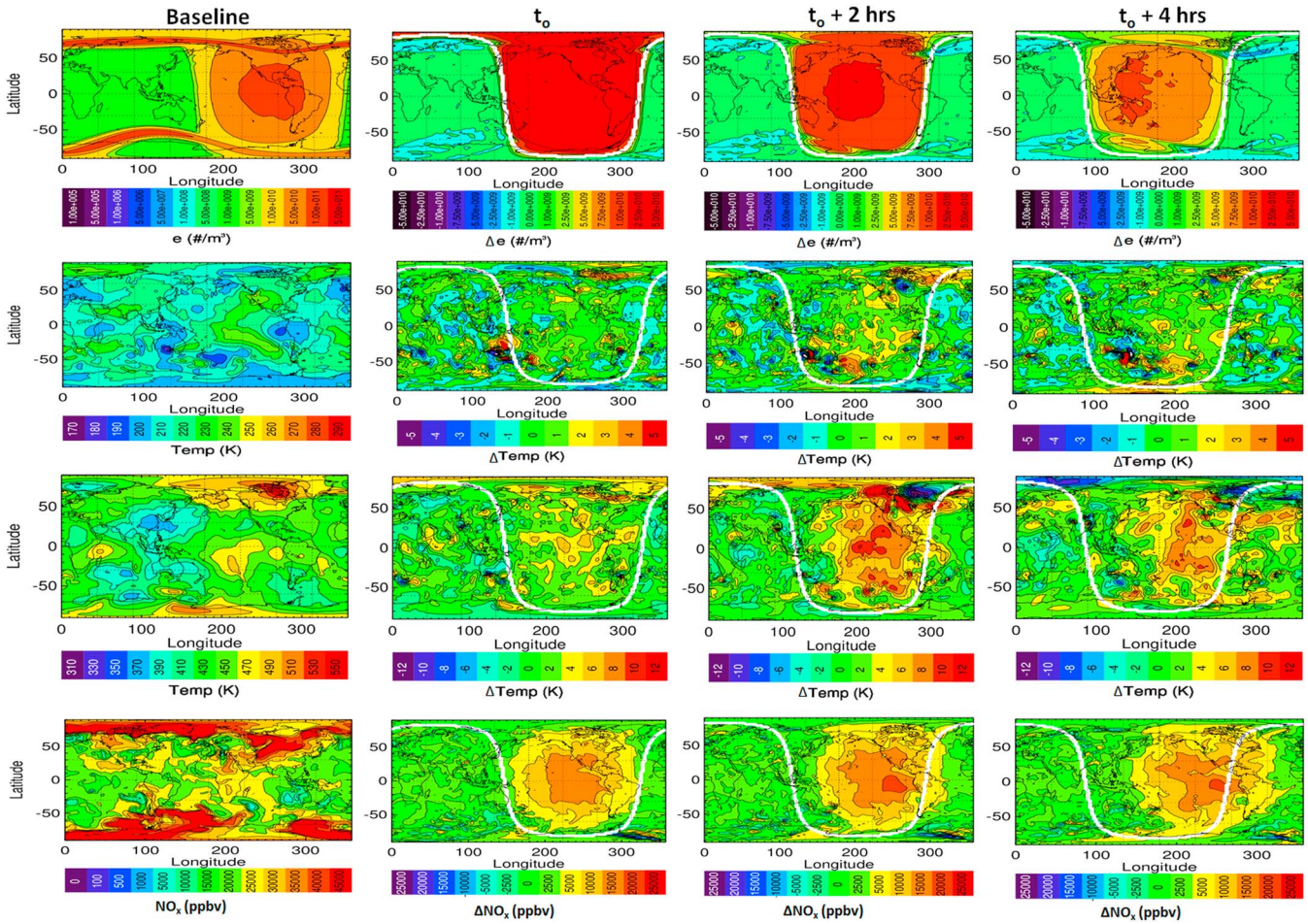

Figure 6. Similar to Figure 5 but for the X-6.2 flare that occurred on 9 September. Also, the baseline simulation background values in column 1 pertain to 19 UT; the difference plots begin at t_0 = 20:30 UT.

on 8 September and peaked on 10 September. The consequent NO_x and HO_x production was most significant in a relative sense from about 1 to 0.01 hPa. NO_x differences greater than 1000% persisted in the lower mesosphere near 0.1 hPa for several hours. The NO_x-rich air descended over the next several weeks, resulting in elevated values until about 20 October at altitudes as low as 3 hPa. HO_x increases also maximized near 0.1 hPa, reaching values of about 30%; as expected, the HO_x enhancements were much shorter lived than the NO_x increases. Flare-induced NO_x increases of about 60% to 80% are evident in the NH polar region around 0.01 hPa, but these differences are much smaller than the increases caused by the SPEs; there were no significant flare-induced HO_x increases. That the SPE effects were much larger than the flare effects at 60–90°N is expected, since particle precipitation effects maximize in the polar region and flare effects maximize at lower latitudes.

SPE- and flare-induced changes in NO_x and HO_x in the SH polar region (60–90°S; Figure 8) are similar in character to those in the NH. However, the SPE-induced NO_x increases are smaller in the SH than in the NH, and the SPE-induced HO_x increases are larger in the SH than in the NH. In addition, the flare-induced NO_x increases appear to be delayed relative to the flare-induced ionization. The different % increases in the NH versus the SH polar regions can be attributed to differences in the baseline NO_x and HO_x values at the end of the winter in the SH and summer in the NH (see, e.g., Jackman et al., 2014). The apparent delay in the NO_x increase is the result of the time required for air with flare-induced NO_x enhancements to descend into regions where these enhancements are significant with respect to the baseline NO_x mixing ratios.

As expected, no SPE influences are evident in the equatorial region from 30°S to 30°N (Figure 9), because the precipitating protons are trapped by the magnetic field lines of Earth and thus are restricted to geomagnetic

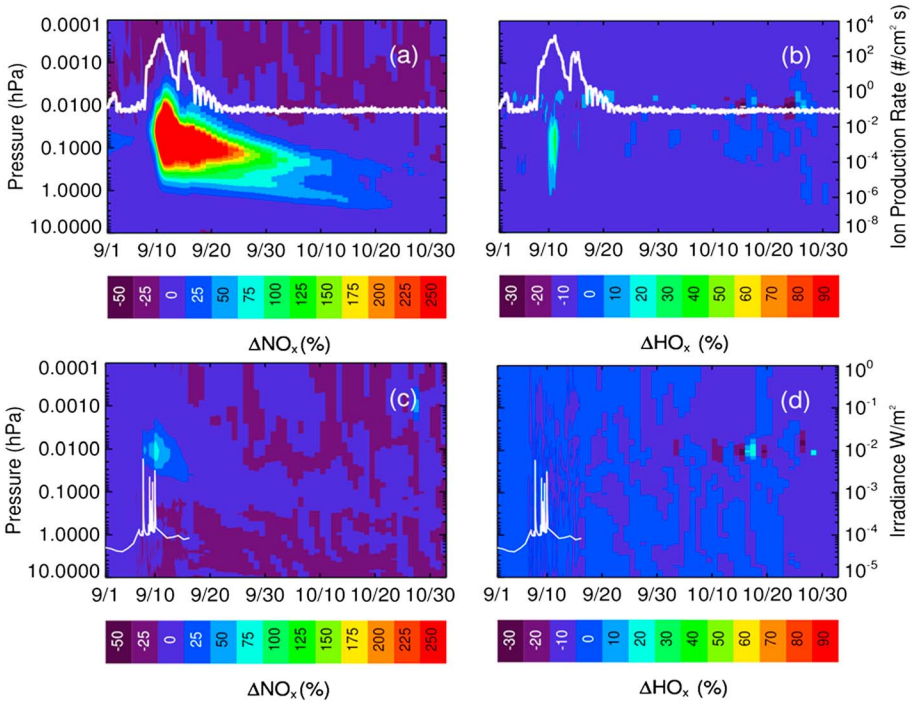

Figure 7. Differences (%) in NO_x (a, c) and HO_x (b, d) mixing ratios between the solar proton event and baseline simulations (a, b; solar proton event minus baseline) and the flare and baseline simulations (c, d; flare minus baseline), in the Northern Hemisphere polar region (60–90°N). White lines show the ionization rate from solar proton events at 0.1 hPa in (a) and (b) and the irradiance at 1.3 nm in (c) and (d).

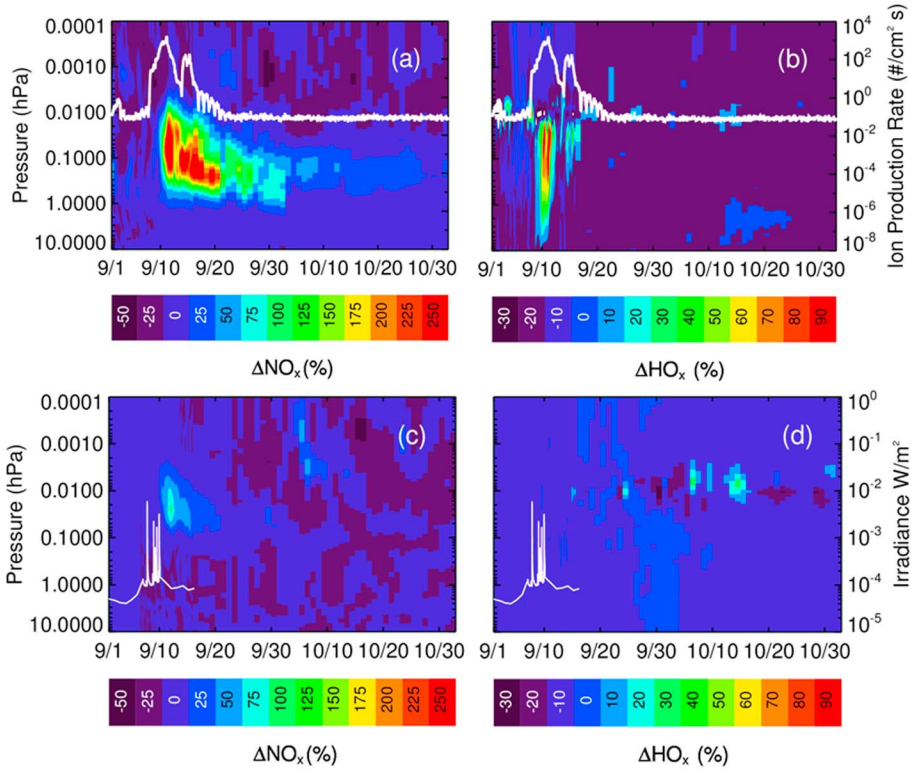

Figure 8. Same as Figure 7 but for the Southern Hemisphere (60–90°S).

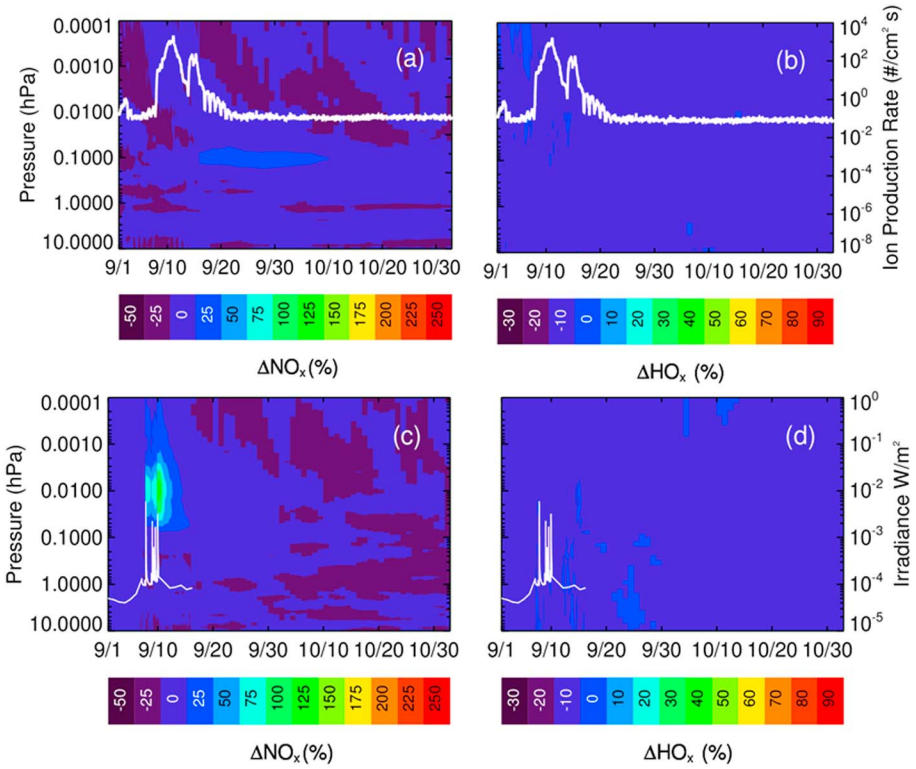

Figure 9. Same as Figure 7 but for the equatorial region (30°S–30°N).

latitudes above 60° in WACCM. The solar flare influence on NO_x, however, is stronger here than in the polar region, with NO_x increases of up to 150% relative to the baseline simulation. Since flare influences only occur on the sunlit side of the Earth, it is expected that the tropics would show the largest NO_x production. The solar flare influence on HO_x in the equatorial region was insignificant relative to the baseline HO_x mixing ratios. This is expected because of the very high baseline HO_x (primarily H) mixing ratios above 0.01 hPa (>5,000 ppmv; not shown) and the short lifetime of HO_x below 0.01 hPa in sunlight (e.g., Pickett et al., 2006). Figure 9 appears to suggest that the 9 September flare had a larger impact on NO_x production than the 7 September flare, but as explained next, this is partially due to the additive effects of relatively long-lived NO_x from previous flares.

To explain why the initial NO_x enhancements after the 9 September flare were larger than after the 7 September flare, even though the opposite was true of the electron density enhancements, Figure 10 compares time series of electron density and NO_x enhancements. Figures 10a and 10b show the electron number density differences between the flare simulations and the baseline simulations. Figure 10a includes the geographic region from 7°S to 7°N latitude and 250°E to 275°E longitude, where the electron density enhancements after the 7 September flare maximized, while Figure 10b includes the geographic region from 7°S to 7°N latitude and 210°E to 235°E longitude, where the electron density enhancements after the 9 September flare maximized. These locations are indicated by black boxes on Figures 5 and 6 for the 7 and 9 September flares, respectively. Figures 10c and 10d show the same regions but for NO_x mixing ratio differences instead. All panels pertain to an altitude of approximately 110 km. The electron differences are very brief and show no cumulative effects; that is, after both flares the electron density increases returned to background values before subsequent flares arrived. However, the NO_x mixing ratio differences show that there are in fact cumulative effects, whereby the NO_x mixing ratios after the 9 September flare include contributions from previous flares. That is, the NO_x mixing ratios had not decayed back to their baseline values before the 9 September flare hit. When calculated relative to the values immediately preceding each flare, the maximum change in NO_x was 1.7×10^4 ppbv for the 7 September flare and 1.4×10^4 ppbv for the 9 September flare. Thus, like the electron densities, the initial NO_x production was smaller after the 9 September flare.

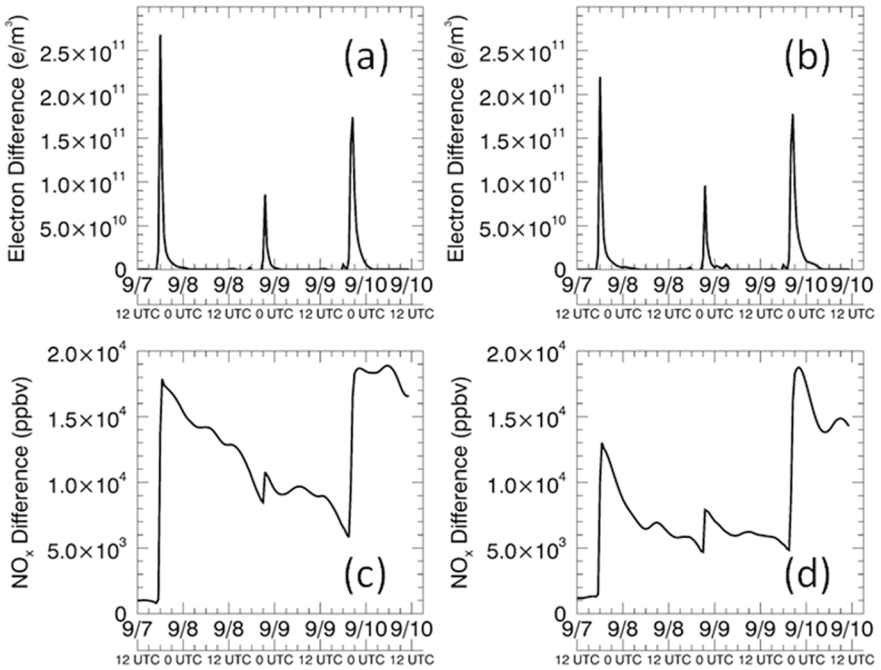

Figure 10. Electron number density differences at 110 km (flare minus baseline) for the geographic region (a) inside the black box in Figure 5 and (b) inside the black box in Figure 6. Panels (c) and (d) show NO_x mixing ratio differences for the same locations as in (a) and (b), respectively.

Quantifying the overall flare impacts on the atmosphere requires examination of not only the initial effects but also the integrated effects. The average electron density enhancements inside the geographic regions indicated by the black boxes in Figures 5 and 6, calculated in 30-min increments over the first 6 hr after the beginning of each of the flares, were 3.79×10^{10} e^-/m^3 for the 7 September flare and 4.82×10^{10} e^-/m^3 for the 9 September flare. This indicates that because the 9 September flare was longer in duration, the total ionization was in fact larger than after the 7 September flare. This result emphasizes the importance of the different spectral characteristics of the two flares. Since the X-6.2 flare on 9 September was stronger during the gradual phase, the enhanced photoionization lasted longer and produced more electrons overall than the X-17 flare on 7 September.

Vertical profiles of the individual NO_x and HO_x components are shown in Figure 11. The top panels (a–c) show differences (fully forced minus baseline) for the various NO_x constituents, and the bottom panels (d–f) show differences for the HO_x constituents. Polar averages from 60°N to 90°N (a, d) and 60°S to 90°S (b, e) correspond to 10 September at 12 UT, near the peak of the SPE. Equatorial averages from 30°S to 30°N (c, f) correspond to 9 September at 21 UT, near the peak of the solar flare on that date. Increases in atomic nitrogen and NO_2 are apparent in all regions, but the vast majority of the increase in NO_x takes the form of NO; in fact, the NO and NO_x curves are nearly indistinguishable in the NH polar region and in the equatorial region. NO_x partitioning shifts toward NO_2 below ~1 hPa in the SH polar region, which is just emerging from the polar night. Indeed, the shift in partitioning from NO to NO_2 increases monotonically with latitude from 60°S to 90°S (not shown), since the pole is still in total darkness at this time of year. SPE-induced HO_x increases take the form of OH throughout much of the ionization region near 0.1 hPa, although HO_2 becomes more significant near 1 hPa in the SH polar region. HO_x partitioning shifts to atomic hydrogen at the highest altitudes at all latitudes (including in the equatorial region where the H and HO_x curves are indistinguishable), consistent with Pickett et al. (2006).

Figure 12 explores the effects of the flares and SPEs on ozone at latitudes from 60°N to 90°N (a) and 60°S to 90°S (b); no significant changes in ozone were discernable in the equatorial region where flare effects are simulated in other species. Ozone decreases of 40–50% in the NH polar region and over 80% in the SH polar region were caused by the SPEs. The ozone decreases were short lived and correspond primarily to increases in HO_x, particularly OH (indicated by the white contour), consistent with well-known HO_x chemistry (Jackman

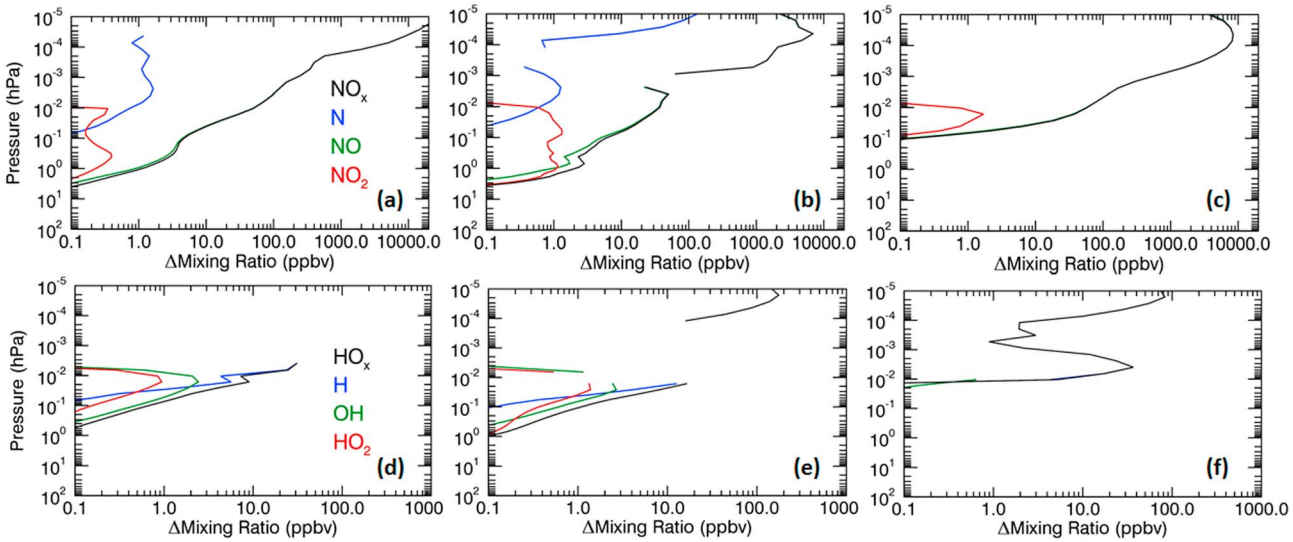

Figure 11. NO_x (top) and HO_x (bottom) constituents for fully forced simulation minus baseline simulation using Northern Hemisphere polar average (a, d), Southern Hemisphere polar average (b, e), and equatorial average (c, f). The polar plots (a, b, d, e) correspond to 10 September at 12 UT (peak of the solar proton event) and the equatorial plots (c, f) correspond to 9 September 21 UT (peak of the flare). Missing lines indicate negative differences between the simulations.

et al., 2008). The model simulations did not reveal any temperature changes that could be ascribed to the HO_x-induced ozone decreases (not shown). Although SPE-induced NO_x enhancements persisted into October in both the NH and SH, the descending NO_x did not reach stratospheric altitudes where NO_x catalytic loss dominates ozone loss. Thus, the EPP indirect effect (Randall et al., 2006) was inconsequential for stratospheric ozone loss, a result that is not surprising since the mesospheric polar vortex in September–October is just forming in the NH and breaking up in the SH.

To evaluate WACCM calculations of NO production by the SPEs and flares, model NO was compared to observations from the Atmospheric Chemistry Experiment Fourier Transform Spectrometer (ACE-FTS) on the Canadian SCISAT-1 satellite (Bernath et al., 2005). ACE-FTS is a solar occultation instrument that measures NO with a vertical resolution of 3–4 km over an altitude range of 6–107 km (Kerzenmacher et al., 2008; Sheese et al., 2016). Figure 13 compares daily mean vertical profiles of WACCM NO mixing ratios (Figure 13a), calculated for the ACE measurement times and locations in the NH, to ACE NO mixing ratio profiles (Figure 13b); note that all of the ACE profiles at these NH latitudes were satellite sunrise occultations. Generally, the NO mixing ratios from WACCM are similar to the ACE mixing ratios. However, WACCM underestimates the mixing ratios relative to ACE during these solar events. On 10 September during the peak of the SPE, ACE shows a larger NO increase near 60–90 km than what WACCM calculates, with differences of

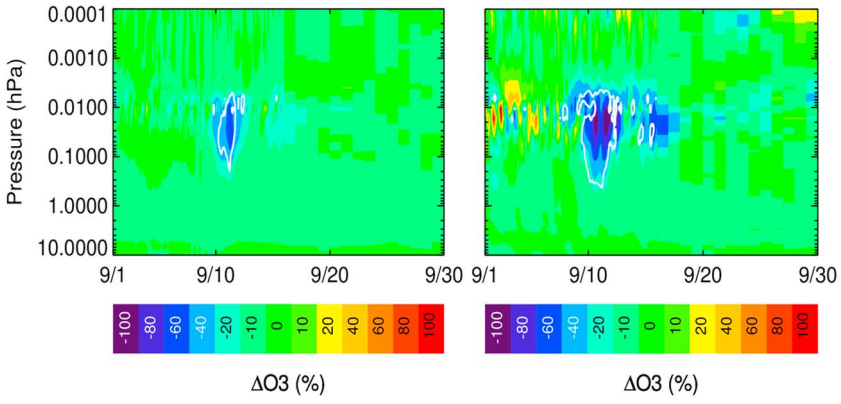

Figure 12. Ozone mixing ratio differences (%) between the fully forced simulation and the baseline simulation (a) from 60°N to 90°N and (b) from 60°S to 90°S. The white contour indicates OH increases of 50%.

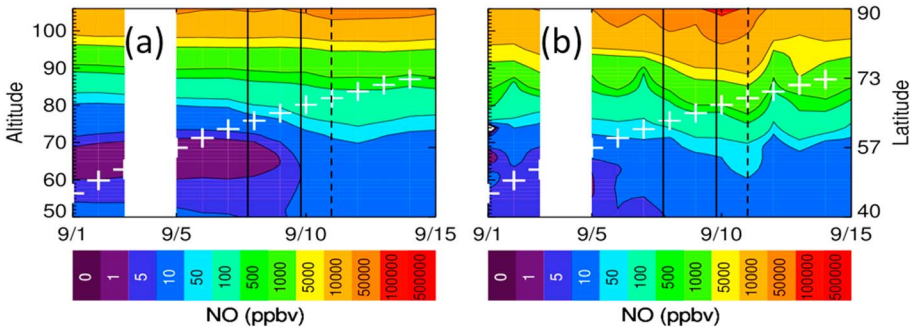

Figure 13. Daily average NO mixing ratios from Whole Atmosphere Community Climate Model at the Atmospheric Chemistry Experiment (ACE) locations and times (a) and NO mixing ratios from ACE (b) for 1–15 September 2005. The ACE measurement latitudes are given by the white plus marks, referenced to the right vertical axis. The solid black vertical lines indicate the X-17 and X-6.2 flares on 7 and 9 September, respectively; the dashed black lines indicate the peak of the solar proton event ionization. White space indicates missing ACE data.

approximately 100 ppbv. At higher altitudes (90–100 km) differences as high as 5,000 ppbv are evident. This result could be due to the omission of medium-energy electrons in the model (e.g., Peck et al., 2015) and is consistent with results from previous studies (Randall et al., 2015).

5. Conclusion

The investigation presented here utilizes new, high-time-cadence solar spectral input in the WACCM coupled chemistry climate model to investigate the effects on the middle atmosphere of solar flares and SPEs during September 2005. Using a 5-min time cadence irradiance input and hourly SPE input, individual WACCM simulations were performed to isolate both solar proton and solar flare effects on middle atmosphere electron production, temperature, and mixing ratios of NO_x, HO_x, and ozone. The flares caused electron number densities to increase by more than 500% in the thermosphere, with largest increases in the equatorial region as expected. Temperature changes were primarily concentrated in the equatorial regions near the subsolar point, with a maximum of 10 K at 125 km during the X-17 flare on 7 September and 12 K at 125 km during the X-6.2 flare on 9 September.

The flares that were investigated in this study differed substantially in both their measured strength and their influence on the atmosphere. The X-17 flare was a fast-rise flare with a shorter decay time than the X-6.2 flare, which had a prolonged decay phase. In addition, the X-17 flare on 7 September was located on the far western limb of the Sun, while the X-6.2 flare on 9 September erupted slightly closer to the center. Consequently, the two flares had remarkably different spectral characteristics. For instance, the smaller flare caused a larger increase of irradiance in the EUV but smaller increase in the X-ray. Wavelengths between 20 and 100 nm tend to deposit energy above WACCM's vertical domain. The first flare had a stronger peak flux in wavelengths less than 20 nm, but the time-integrated flux over the following 4 hr was close to the same. The peak fluxes at wavelengths longer than 20 nm were higher in the 9 September flare. The 7 September flare caused a larger initial increase in electron density as well as NO_x production at the peak of the flare. In contrast, the time-integrated effects of the 9 September flare were larger. Spectral variability has a large impact on the flare influence on the atmosphere. Effects by X-ray flux are well represented in WACCM, but some of the EUV effects will be at altitudes above 140 km and thus cannot be simulated by WACCM. This suggests that simulations of the smaller flare on 9 September would show even more atmospheric impacts if the EUV radiation outside the model's domain could be represented. The upcoming release of WACCM-X will solve this problem by expanding the model vertical domain to 500 km.

The simulations show that the SPEs had a much larger impact on NO_x and HO_x in the polar mesosphere than any of the flares. The SPEs caused increases of more than 1,000% in NO_x in the polar mesosphere, with enhancements of at least 25% persisting into mid-October. SPE-induced HO_x increases reached 90% in the SH polar mesosphere and about 30% in the NH polar mesosphere but were short lived; the hemispheric differences were attributed primarily to differences in the background HO_x values. Short-lived ozone loss of up to ~50% in the NH polar lower mesosphere and over 80% in the SH polar lower mesosphere was attributed to

the SPE-produced HO_x. No changes in temperature could be ascribed to this ozone loss. Longer-lived ozone loss from the EPP indirect effect was not evident in the simulations because the SPE-produced NO_x did not descend to the stratospheric altitudes most relevant for the NO_x catalytic cycle. Had the SPEs studied in this work occurred in midwinter instead of in September, significant ozone loss from the EPP indirect effect would have been more likely (e.g., Jackman et al., 2008). Since solar protons precipitate in the polar regions, the SPEs did not perturb the equatorial mesosphere nor did they significantly impact the thermosphere, even in the polar regions, since their energy was deposited primarily in the mesosphere.

Relative to the SPEs, the flares caused more modest and shorter-lived NO_x increases in the polar mesosphere; flare-induced NO_x enhancements of 60–80% decayed to less than 25% by around 20 September. The flares caused NO_x mixing ratio increases of several thousand parts per billion by volume in both the tropical and polar thermosphere, but these increases represented relative changes of less than 25%. The work presented here demonstrates for the first time the ability of a fully coupled climate model such as WACCM to simulate solar flare effects on the middle atmosphere using very high time resolution for the flare spectral input. While there were significant flare-induced increases in electron density and odd nitrogen in the mesosphere, the flares did not significantly impact mesospheric HO_x or ozone and did not affect the stratosphere.

Acknowledgments
This research has been funded by the NASA Living With a Star program, grant NNX14AH54G and by the NSF Frontiers of Earth System Dynamics program, grant AGS 1135432. We thank NCAR for the use of the WACCM model as well as their high-performance computing. The National Center for Atmospheric Research is operated by the University Corporation for Atmospheric Research under sponsorship of the National Science Foundation. We would also like to thank MIT Haystack for their GPS TEC data.

References

Afraimovich, E. L., Altynsev, A. T., Grechnev, V. V., & Leonovich, L. A. (2001). Ionospheric effects of the solar flares deduced from global GPS network data. *Advances in Space Research*, *27*, 1333–1338. https://doi.org/10.1016/S0273-1177(01)00172-7

Afraimovich, E. L., Altyntsev, A. T., Kosogorov, E. A., Larina, N. S., & Leonovich, L. A. (2001). Ionospheric effects of the solar flares of September 23, 1998 and July 29, 1999 as deduced from global GPS network data. *Journal of Atmospheric and Solar: Terrestrial Physics*, *63*, 1841–1849. https://doi.org/10.1016/S1364-6826(01)00060-8

Bastian, T. (2010). Radiative signatures of energetic particles. In C. J. Schrijver & G. L. Siscoe (Eds.), *Heliophysics: Space storms and radiation: Causes and effects* (pp. 79–123). Cambridge: Cambridge University Press.

Bernath, P. F., McElroy, T., Abrams, M. C., Boone, C. D., Butler, M., Camy-eyret, C., et al. (2005). Atmospheric Chemistry Experiment (ACE): Mission overview. *Geophysical Research Letters*, *32*, L15S01. https://doi.org/10.1029/2005GL022386

Brakebusch, M., Randall, C. E., Kinnison, D. E., Tilmes, S., Santee, M. L., & Manney, G. L. (2013). Evaluation of Whole Atmosphere Community Climate Model simulations of ozone during Arctic winter 2004–2005. *Journal of Geophysical Research: Atmospheres*, *118*, 2673–2688. https://doi.org/10.1002/jgrd.50226

Chamberlin, P. C., Woods, T. N., & Eparvier, F. G. (2007). Flare Irradiance Spectral Model (FISM): Daily component algorithms and results. *Space Weather*, *5*, S07005. https://doi.org/10.1029/2007SW000316

Chamberlin, P. C., Woods, T. N., & Eparvier, F. G. (2008). Flare Irradiance Spectral Model (FISM): Flare component algorithms and results. *Space Weather*, *6*, S05001. https://doi.org/10.1029/2007SW000372

Crutzen, P. J., Isaksen, I. S. A., & Reid, G. C. (1975). Solar proton events: Stratospheric sources of nitric oxide. *Science*, *189*, 457–459. https://doi.org/10.1126/science.189.4201.457

Donnelly, R. F. (1976). Empirical models of solar flare X-ray and EUV emissions for use in studying their *E* and *F* region effects. *Journal of Geophysical Research*, *81*, 4745–4753. https://doi.org/10.1029/JA081i025p04745

Enell, C.-F., Verronen, P. T., Beharrell, M. J., Vierinen, J. P., Kero, A., Seppälä, A., et al. (2008). Case study of the mesospheric and lower thermospheric effects of solar X-ray flares: Coupled ion-neutral modelling and comparison with EISCAT and riometer measurements. *Annales Geophysicae*, *26*, 2311–2321. https://doi.org/10.5194/angeo-26-2311-2008

Eyring, V., Arblaster, J. M., Cionni, I., Sedláček, J., Perlwitz, J., Young, P. J., et al. (2013). Long-term ozone changes and associated climate impacts in CMIP5 simulations. *Journal of Geophysical Research: Atmospheres*, *118*, 5029–5060. https://doi.org/10.1002/jgrd.50316

Fuller-Rowell, T. J., & Solomon, S. C. (2010). Flares, coronal mass ejections, and atmospheric responses. In C. J. Schrijver & G. L. Siscoe (Eds.), *Heliophysics: Space storms and radiation: Causes and effects* (pp. 321–357). Cambridge: Cambridge University Press.

Funke, B., Baumgaertner, A., Calisto, M., Egorova, T., Jackman, C. H., Kieser, J., et al. (2011). Composition changes after the "Halloween" solar proton event: The High Energy Particle Precipitation in the Atmosphere (HEPPA) model versus MIPAS data intercomparison study. *Atmospheric Chemistry and Physics*, *11*, 9089–9139. https://doi.org/10.5194/acp-11-9089-2011

Gopalswamy, N., Yashiro S., & Akiyama S. (2006). Coronal mass ejections and space weather due to extreme events. Paper presented at ILWS Workshop, Goa, India.

Heyvaerts, J., Priest, E. R., & Rust, D. M. (1977). An emerging flux model for the solar flare phenomenon. *Astrophysical Journal*, *216*, 123–127. https://doi.org/10.1086/155453

Huang, Y. S., Richmond, A. D., Deng, Y., Chamberlin, P. C., Qian, L., Solomon, S. C., et al. (2013). Wavelength dependence of solar irradiance enhancement during X-class flares and its influence on the upper atmosphere. *Journal of Atmospheric and Solar: Terrestrial Physics*, *115-116*, 87–94. https://doi.org/10.1016/j.jastp.2013.10.011

Huba, J. D., Warren, H. P., Joyce, G., Pi, X., Iijima, B., & Coker, C. (2005). Global response of the low-latitude to midlatitude ionosphere due to the Bastille Day flare. *Geophysical Research Letters*, *32*, L15103. https://doi.org/10.1029/2005GL023291

Hudson, H. (2010). Observations of solar and stellar eruptions, flares, and jets. In C. J. Schrijver & G. L. Siscoe (Eds.), *Heliophysics: Space storms and radiation: Causes and effects* (pp. 123–159). Cambridge: Cambridge University Press.

Hurrell, J. W., Holland, M. M., Gents, P. R., Ghan, S., Kay, J. E., Kushner, P. J., et al. (2013). The Community Earth System Model: A framework for collaborative research. *Bulletin of the American Meteorological Society*, *94*, 1339–1360. https://doi.org/10.1175/BAMS-D-12-00121.1

Jackman, C. H., Cerniglia, M. C., Nielsen, E. J., Allen, D. J., Zawodny, J. M., McPeters, R. D., et al. (1995). Two-dimensional and three-dimensional model simulations, measurements and interpretation of the influence of the October 1989 solar proton events on the middle atmosphere. *Journal of Geophysical Research*, *100*, 11,641–11,660. https://doi.org/10.1029/95JD00369

Jackman, C. H., DeLand, M. T., Labow, G. J., Fleming, E. L., & Lopez-Puertas, M. (2006). Satellite measurements of middle atmospheric impacts by solar proton events in solar cycle 23. *Space Science Reviews*, *125*, 381–391. https://doi.org/10.1007/s11214-006-9071-4

Jackman, C. H., DeLand, M. T., Labow, G. J., Fleming, E. L., Weisenstein, D. K., Ko, M., et al. (2005). The influence of the several very large solar proton events in years 2000–2003 on the neutral middle atmosphere. *Advances in Space Research*, *35*, 445–450. https://doi.org/10.1016/j.asr.2004.09.006

Jackman, C. H., Frederick, J. E., & Stolarski, R. S. (1980). Production of odd nitrogen in the stratosphere and mesosphere: An intercomparison of source strengths. *Journal of Geophysical Research*, *85*, 7495–7505. https://doi.org/10.1029/JC085iC12p07495

Jackman, C. H., Marsh, D. R., Vitt, F. M., Garcia, R. R., Fleming, E. L., Labow, G. J., et al. (2008). Short and medium-term atmospheric constituent effects of very large solar proton events. *Atmospheric Chemistry and Physics*, *8*, 765–785. https://doi.org/10.5194/acp-8-765-2008

Jackman, C. H., Marsh, D. R., Vitt, F. M., Garcia, R. R., Randall, C. E., Fleming, E. L., & Frith, S. M. (2009). Long-term middle atmospheric influence of very large solar proton events. *Journal of Geophysical Research*, *114*, D11304. https://doi.org/10.1029/2008JD011415

Jackman, C. H., Randall, C. E., Harvey, V. L., Wang, S., Fleming, E. L., Lopez-Puertas, M., et al. (2014). Middle atmospheric changes caused by the January and March 2012 solar proton events. *Atmospheric Chemistry and Physics*, *14*, 1025–1038. https://doi.org/10.5194/acp-14-1025-2014

Kerzenmacher, T., Wolff, M. A., Strong, K., Dupuy, E., Walker, K. A., Amekudzi, L. K., et al. (2008). Validation of NO_2 and NO from the Atmospheric Chemistry Experiment (ACE). *Atmospheric Chemistry and Physics*, *8*, 5801–5841. https://doi.org/10.5194/acp-8-5801-2008

Kinnison, D. E., Brasseur, G. P., Walters, S., Garcia, R. R., Marsh, D. R., Sassi, F., et al. (2007). Sensitivity of chemical tracers to meteorological parameters in the MOZART-3 chemical transport model. *Journal of Geophysical Research: Atmospheres*, *112*, D20302. https://doi.org/10.1029/2006JD007879

Lanzerotti, L. J. (2013). Space weather effects on technologies. In P. Song, H. J. Singer, & G. L. Siscoe (Eds.), *Space Weather, Geophysical Monograph Series* (Vol. 125, pp. 39–44). Washington, DC: American Geophysical Union.

Le, H., Liu, L., Chen, B., Lei, J., Yue, X., & Wan, W. (2007). Modeling the responses of the middle latitude ionosphere to solar flares. *Journal of Atmospheric and Solar: Terrestrial Physics*, *69*, 1587–1598. https://doi.org/10.1016/j.jastp.2007.06.005

Le, H., Liu, L., He, H., & Wan, W. (2011). Statistical analysis of solar EUV and X-ray flux enhancements induced by solar flares and its implication to upper atmosphere. *Journal of Geophysical Research*, *116*, A11301. https://doi.org/10.1029/2011JA016704

Le, H., Liu, L., Ren, Z., Chen, Y., Zhang, H., & Wan, W. (2016). A modeling study of global ionospheric and thermospheric responses to extreme solar flare. *Journal of Geophysical Research: Space Physics*, *121*, 832–840. https://doi.org/10.1002/2015JA021930

Liu, J. Y., Lin, C. H., Chen, Y. I., Lin, Y. C., Fang, T. W., Chen, C. H., et al. (2006). Solar flare signatures of the ionospheric GPS total electron content. *Journal of Geophysical Research*, *111*, A05308. https://doi.org/10.1029/2005JA011306

López-Puertas, M., Funke, B., Gil-Lopez, S., von Clarmann, T., Stiller, G. P., Höpfner, M., et al. (2005). HNO_3, N_2O_5, and $ClONO_2$ enhancements after the October–November 2003 solar proton events. *Journal of Geophysical Research*, *110*, A09S44. https://doi.org/10.1029/2005JA011051

Marsh, D. R., Mills, M. J., Kinnison, D. E., Lamarque, J. F., Calvo, N., & Polvani, L. M. (2013). Climate change from 1850 to 2005 simulated in CESM1 (WACCM). *Journal of Climate*, *26*, 7372–7391. https://doi.org/10.1175/JCLI-D-12-00558.1

Matthes, K., Funke, B., Andersson, M. E., Barnard, L., Beer, J., Charbonneau, P., et al. (2017). Solar forcing for CMIP6 (v3.2). *Geoscientific Model Development*, *10*, 2247–2302. https://doi.org/10.5194/gmd-10-2247-2017

Meier, R. R., Warren, H. P., Nicholas, A. C., Bishop, J., Huba, J. D., Drob, D. P., et al. (2002). Ionospheric and dayglow responses to the radiative phase of the Bastille Day flare. *Geophysical Research Letters*, *29*(10), 1461. https://doi.org/10.1029/2001GL013956

Pawlowski, D. J., & Ridley, A. J. (2011). The effects of different solar flare characteristics on the global thermosphere. *Journal of Atmospheric and Solar: Terrestrial Physics*, *73*, 1840–1848. https://doi.org/10.1016/j.jastp.2011.04.004

Peck, E. D., Randall, C. E., Green, J. C., Rodriguez, J. V., & Rodger, C. J. (2015). POES MEPED differential flux retrievals and electron channel contamination correction. *Journal of Geophysical Research: Space Physics*, *120*, 4596–4612. https://doi.org/10.1002/2014JA020817

Pickett, H. M., Read, W. G., Lee, K. K., & Yung, Y. L. (2006). Observation of night OH in the mesosphere. *Geophysical Research Letters*, *33*, L19808. https://doi.org/10.1029/2006GL026910

Qian, L., Burns, A. G., Chamberlin, P. C., & Solomon, S. C. (2010). Flare location on the solar disk: Modeling the thermosphere and ionosphere response. *Journal of Geophysical Research*, *115*, A09311. https://doi.org/10.1029/2009JA015225

Qian, L., Burns, A. G., Chamberlin, P. C., & Solomon, S. C. (2011). Variability of thermosphere and ionosphere responses to solar flares. *Journal of Geophysical Research*, *116*, A10309. https://doi.org/10.1029/2011JA016777

Randall, C. E., Bevilacqua, R. M., Rusch, D. W., Hoppel, K. W., & Lumpe, J. D. (1998). POAM II measurements of NO_2, 1993–1996. *Journal of Geophysical Research*, *103*(D21), 28,361–28,371. https://doi.org/10.1029/98JD02092

Randall, C. E., Harvey, V. L., Holt, L. A., Marsh, D. R., Kinnison, D., Funke, B., & Bernath, P. F. (2015). Simulation of energetic particle precipitation effects during the 2003–2004 Arctic winter. *Journal of Geophysical Research: Space Physics*, *120*, 5035–5048. https://doi.org/10.1002/2015JA021196

Randall, C. E., Harvey, V. L., Manney, G. L., Orsolini, Y., Codrescu, M., Sioris, C., et al. (2005). Stratospheric effects of energetic particle precipitation in 2003–2004. *Geophysical Research Letters*, *32*, L05802. https://doi.org/10.1029/2004GL02203

Randall, C. E., Harvey, V. L., Singleton, C. S., Bernath, P. F., Boone, C. D., & Kozyra, J. U. (2006). Enhanced NO_x in 2006 linked to strong upper stratospheric Arctic vortex. *Geophysical Research Letters*, *33*, L18811. https://doi.org/10.1029/2006GL027160

Randall, C. E., Siskind, D. E., & Bevilacqua, R. M. (2001). Stratospheric NO_x enhancements in the Southern Hemisphere vortex in winter/spring of 2000. *Geophysical Research Letters*, *28*(12), 2385–2388. https://doi.org/10.1029/2000GL012746

Rienecker, M. M., Suarez, M. J., Gelaro, R., Todling, R., Bacmeister, J., Liu, E., et al. (2011). MERRA: NASA's Modern-Era Retrospective Analysis for Research and Applications. *Journal of Climate*, *24*, 3624–3648. https://doi.org/10.1175/JCLI-D-11-00015.1

Roble, R. G., & Ridley, E. C. (1987). An auroral model for the NCAR thermospheric general circulation model (TGCM). *Annales Geophysicae*, *5A*(6), 369–382.

Rottman, G. J., Woods, T. N., & Sparn, T. P. (1993). Solar Stellar Irradiance Comparison Experiment I: 1 instrument design and operation. *Journal of Geophysical Research*, *98*, 10,667–10,677. https://doi.org/10.1029/93JD00462

Schrijver, C. J. (2009). Driving major solar flares and eruptions: A review. *Advances in Space Research*, *43*, 739–755. https://doi.org/10.1016.j.asr.2008.11.004

Sheese, P. E., Walker, K. A., Boone, C. D., McLinden, C. A., Bernath, P. F., Bourassa, A. E., et al. (2016). Validation of ACE-FTS version 3.5 NO_y species profiles using correlative satellite measurements. *Atmospheric Measurement Techniques*, *9*, 5781–5810. https://doi.org/10.5194/amt-9-5781-2016

Shibata, K., & Magara, T. (2011). Solar flares: Magnetohydrodynamic processes. *Living Reviews in Solar Physics*, *8*, 6. https://doi.org/10.12942/lrsp-2011-6

Sinnhuber, M., Nieder, Y., & Wieters, N. (2012). Energetic particle precipitation and the chemistry of the mesosphere/lower thermosphere. *Surveys in Geophysics*, *33*, 1281–1334. https://doi.org/10.1007/s10712-012-9201-3

Solomon, S., Crutzen, P. J., & Roble, R. G. (1982). Photochemical coupling between the thermosphere and the lower atmosphere: 1. Odd nitrogen from 50 to 120 km. *Journal of Geophysical Research*, *87*(C9), 7206–7220. https://doi.org/10.1029/JC087iC09p07206

Solomon, S., Rusch, D. W., Gérard, J. C., Reid, G. C., & Crutzen, P. J. (1981). The effect of particle precipitation events on the neutral and ion chemistry of the middle atmosphere: II. Odd hydrogen. *Planetary and Space Science*, *29*(8), 885–893. https://doi.org/10.1016/0032-0633(81)90078-7

Solomon, S. C., Kinnison, D., Bandoro, J., & Garcia, R. (2015). Simulation of polar ozone depletion: An update. *Journal of Geophysical Research: Atmospheres*, *120*, 7958–7974. https://doi.org/10.1002/2015JD023365

Solomon, S. C., & Qian, L. (2005). Solar extreme-ultraviolet irradiance for general circulation models. *Journal of Geophysical Research*, *110*, A10306. https://doi.org/10.1029/2005JA011160

Thorne, R. M. (1980). The importance of energetic particle precipitation on the chemical composition of the middle atmosphere. *Pure and Applied Geophysics*, *118*, 128–151.

Tsurutani, B. T., Judge, D. L., Guarnieri, F. L., Gangopadhyay, P., Jones, A. R., Nuttall, J., et al. (2005). The October 28, 2003 extreme EUV solar flare and resultant extreme ionospheric effects: Comparison to other Halloween events and the Bastille Day event. *Geophysical Research Letters*, *32*, L03S09. https://doi.org/10.1029/2004GL021475

Tsurutani, B. T., Verkhoglyadova, O. P., Mannucci, A. J., Lakhina, G. S., Li, G., & Zank, G. P. (2009). A brief review of "solar flare effects" on the ionosphere. *Radio Science*, *44*, RS0A17. https://doi.org/10.1029/2008RS004029

Turner, R. (2013). What we must known about solar particle events to reduce the risk of astronauts. In P. Song, H. J. Singer, & G. L. Siscoe (Eds.), *Space Weather, Geophysical Monograph Series* (Vol. 125, pp. 39–44). Washington, DC: American Geophysical Union.

Vitt, F. M., & Jackman, C. H. (1996). A comparison of sources of odd nitrogen production from 1974 through 1993 in the Earth's atmosphere as calculated using a two-dimensional model. *Journal of Geophysical Research*, *101*, 6729–6739. https://doi.org/10.1029/95JD03386

Woods, T. N., Bailey, S., Solomon, S., Rottman, G., & Worden, J. (1994). Recent solar EUV irradiance measurements. Boulder, CO: Front Range American Geophysical Union.

Woods, T. N., Eparvier, F. G., Fontenla, J., Harder, J., Kopp, G., McClintock, W. E., et al. (2004). Solar irradiance variability during the October 2003 solar storm period. *Geophysical Research Letters*, *31*, L10802. https://doi.org/10.1029/2004GL019571